Determination of Klinkenberg Permeability Conditioned to Pore-Throat Structures in Tight Formations

Guangfeng Liu [1,*] (ID)**, Yaoxing Bai** [2] (ID)**, Zhaoqi Fan** [3] **and Daihong Gu** [1]

[1] CMOE Key Laboratory of Petroleum Engineering, China University of Petroleum-Beijing, Beijing 102249, China; gudaihong@cup.edu.cn

[2] Shanxi Natural Gas Limited Company, Taiyuan, Shanxi 030002, China; baiyaoxing@sina.com

[3] Petroleum Systems Engineering, Faculty of Engineering and Applied Science, University of Regina, Regina, SK S4S 0A2, Canada; fan240@uregina.ca

* Correspondence: lgf@cup.edu.cn; Tel.: +86-10-8973-2192

Abstract: This paper has developed a pragmatic technique to efficiently and accurately determine the Klinkenberg permeability for tight formations with different pore-throat structures. Firstly, the authors use steady-state experiments to measure the Klinkenberg permeability of 56 tight core samples under different mean pore pressures and confining pressures. Secondly, pressure-controlled mercury injection (PMI) experiments and thin-section analyses are conducted to differentiate pore-throat structures. After considering capillary pressure curve, pore types, throat size, particle composition, and grain size, the pore-throat structure in the target tight formation was classified into three types: a good sorting and micro-fine throat (GSMFT) type, a moderate sorting and micro-fine throat (MSMFT) type, and a bad sorting and micro throat (BSMT) type. This study found that a linear relationship exists between the Klinkenberg permeability and measured gas permeability for all three types of pore-throat structures. Subsequently, three empirical equations are proposed, based on 50 core samples of data, to estimate the Klinkenberg permeability by using the measured gas permeability and mean pore pressure for each type of pore-throat structure. In addition, the proposed empirical equations can generate accurate estimates of the Klinkenberg permeability with a relative error of less than 5% in comparison to its measured value. The application of the proposed empirical equations to the remaining six core samples has demonstrated that it is necessary to use an appropriate equation to determine the Klinkenberg permeability of a specific type of pore-throat structure. Consequently, the newly developed technique is proven to be qualified for accurately determining the Klinkenberg permeability of tight formations in a timely manner.

Keywords: tight formation; Klinkenberg permeability; gas permeability; pore-throat structure

1. Introduction

With the escalating demands of crude oil and natural gas, unconventional resources have attracted numerous attentions as a surrogate of conventional reserves [1], although the oil price suffers. The magnitude of the permeability in a tight formation plays a significant role in optimizing its development strategies. Since the measured gas permeability varies with gas types and experimental conditions, the absolute permeability is conventionally employed to characterize the petrophysical property of a specific tight formation [2]. In general, the absolute permeability is represented by Klinkenberg permeability, which is determined by extrapolating the measured gas permeability versus mean pore pressure curve to the infinite pressure point [3]. The approaches to examining the Klinkenberg permeability have found limitations in tight formations due to the presence of

complex pore-throat structures and complicated flow principles [4,5]. Therefore, it is of practical and fundamental importance to develop a method for accurately determining the Klinkenberg permeability for tight formations characterized by various pore-throat structures.

The differences between the measured gas permeability and the Klinkenberg permeability can be attributed to the slippage effect, which is involved when the mean free path of the measured gas is greater than pore- or throat-diameters [6]. In addition, the difference between the measured water permeability and the Klinkenberg permeability also exists, which is caused by a slip effect induced by a strongly hydrophobic wall of nanopores [7]. Substantial efforts have been made to depict such differences by using empirical correlations that would be practical tools for the efficient estimation of the absolute permeability [2,8,9]. Recently, different correlations with different overburden pressures have been established in the form of power functions between water permeability and Klinkenberg corrected gas permeability for the Upper and Lower Shuaiba Formation [10]. Those correlations moderately reflect the influences of heterogeneity and lithofacies on the Klinkenberg permeability. In addition, the adsorbed gas widely exists in shale gas, including tight sandstone gas, due to a narrow pore throat at nanoscale; thus, the surface diffusion may contribute to gas transports in tight formation [11,12]. Slippage effect measurements of shale reveal that the pore-throat size of the unconventional reservoir, with nano- to micro- pore-throat systems, substantially contributes to the Klinkenberg permeability [13].

Physically, the slippage effect originates from the difference between the mean free path of gases and the distribution of pore-throat systems [6,14]. As such, the absolute permeability is greatly affected by the pore-throat aperture, especially in tight sandstone reservoirs [15]. Although the quantitative relationship between the pore-throat structure and the absolute permeability is not available, it has been reported that both the slippage effect and the absolute permeability are dramatically affected by the pore-throat structure [16–18]. Dong et al. demonstrated that the slippage effect is more remarkable in smaller throats by comparing volcanic core samples with similar permeabilities, but different throat size distributions [19]. The depositional environments result in complicated throat size distributions in a tight formation, which implies that the contribution of the slippage effect to the absolute permeability would significantly change in distinct pore-throat systems [20,21]. Nevertheless, no attempts have been made to determine the absolute/Klinkenberg permeability of a tight formation conditioned to its pore-throat systems.

In this paper, a pragmatic technique has been developed to determine Klinkenberg permeability in a tight formation by considering the pore-throat structure, mean pore pressure, and measured gas permeability. Experimentally, gas permeabilities of 56 core samples collected from a tight reservoir in China are measured by using steady-state experiments. Then, the pore structures characterized by pore-throat sorting coefficient, mercury entry pressure, median saturation pressure, mean throat radius, and maximum mercury injection saturation are measured through pressure-controlled mercury injection (PMI) experiments. The pore types and grain size distribution are also measured by use of thin section analyses. Subsequently, all of the measurements are used to classify the pore-throat structure in the given tight formation and to derive empirical equations for determining the Klinkenberg permeability of different types of pore-throat structures. Finally, a Klinkenberg permeability-measured gas permeability chart is established after the validation of the derived empirical equations.

2. Experimental

2.1. Materials

Figure 1 shows the object of this work, i.e., the Upper Triassic Yanchang Formation of the Chang 7 tight oil reservoir located in Ordos Basin, China, from which 56 tight sandstone samples with gas permeability lower than 0.500 mD are collected. Cylindrical core samples with a diameter of 25 mm and a length of more than 50.8 mm are drilled parallel to the bedding from the collected full-size cores with no fractures or vugs. It is worthwhile noting that residual oil has been removed from

all of the core samples by following the standard GB/T29172-2012 [22] to improve the accuracy of the permeability measurement. Nitrogen is a common gas for measuring gas permeability, while helium can improve the accuracy of the porosity measurement, because it can enter smaller pores and throats due to its small molecular volume. In the present work, helium and nitrogen with a purity of 99.999 vol % are used in porosity and permeability measurements, respectively.
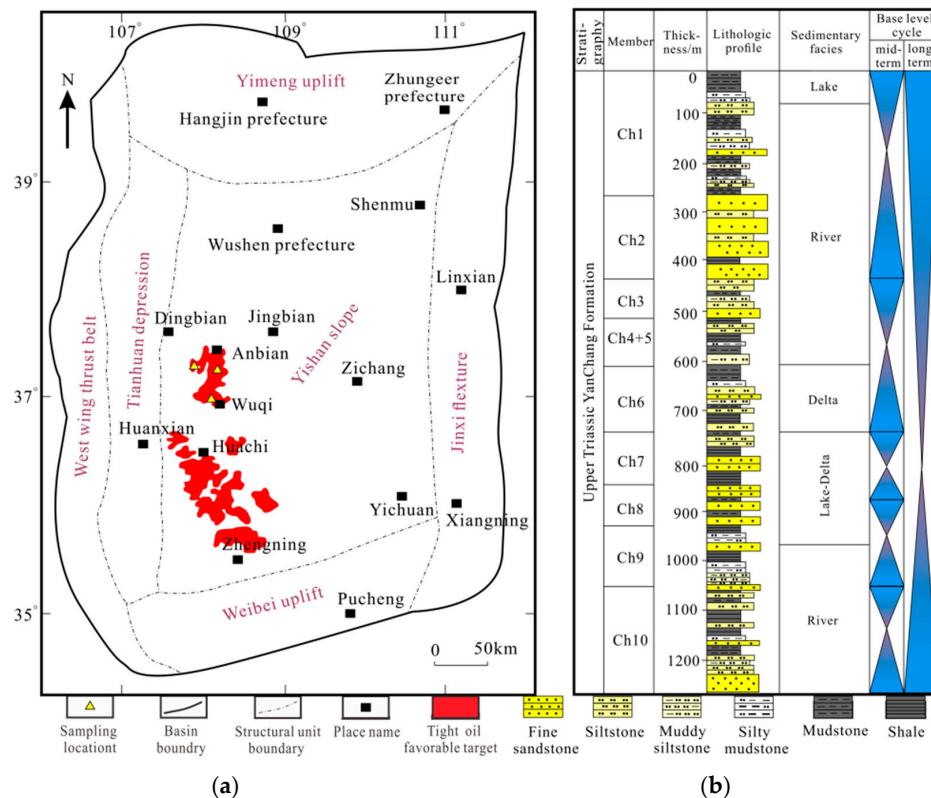

(**a**) (**b**)

Figure 1. (**a**) Tectonic divisions and tight oil favorable target of Ordos basin, and (**b**) Stratigraphic column of the Yanchang Formation (Revised from Wang et al. and Liu et al. [23,24]).

2.2. Experimental Setup

Gas permeability measurements at different mean pore pressures were performed by using the experimental setup as shown in Figure 2, which consists of four subsystems: an injection subsystem, a physical model subsystem, a production subsystem, and a temperature control subsystem.
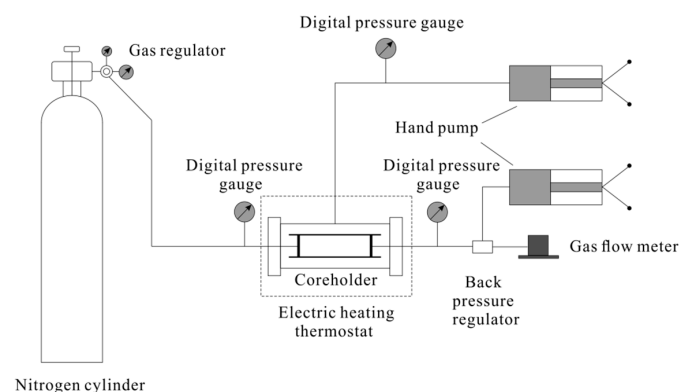

Figure 2. Schematic diagram of the experimental setup.

The injection subsystem includes a nitrogen cylinder, a gas regulator, and a digital pressure gauge to provide continuous nitrogen to the physical model subsystem. A core plug is placed inside a core holder (HZ-MX16, Xi'an, China) with a maximum operating pressure of 50.00 MPa. A high-pressure hand pump (JB-II, Hai'an, Nantong, China) is used to supply the confining pressure to the core holder. The applied confining pressure is set to be 2.00 MPa higher than the inlet pressure for all experiments in order to minimize the stress dependence of Klinkenberg permeability [25]. The production subsystem is comprised of a digital pressure gauge (3051S, ROSEMOUNT, Chanhassen, MN, USA) with the accuracy of 0.025% FS, and a maximum operating pressure of 2.07 MPa, a back pressure regulator (BPR) (HY-2, Nantong, China), and a gas flow meter (50 sccm, ALICAT, Tucson, AZ, USA) with the accuracy of ± (0.8% RDG + 0.2% F.S). Another hand pump is applied to exert pressure on the BPR, which is used to maintain a pre-specified pressure inside the physical model during an individual test. The produced gas is measured by the gas flow meter before being exhausted to the atmosphere. Constant experimental temperature is maintained to be 25.0 °C by using the temperature control subsystem, i.e., an electric heating thermostat (WH-TH-408L, Nantong, China). The thin section analysis was performed with a Nikon ECLIPSE LV100POL polarizing microscope. In addition, a PoreMasterAutoPore IV 9500 (MICROMERITICS INSTRUMENT CORP, Atlanta, GA, USA) mercury porosimeter was used to implement a pressure-controlled mercury injection (PMI) tests for all core samples.

2.3. Experimental Procedures

Two-stage experiments have been designed to determine the Klinkenberg permeability conditioned to pore-throat structures. In Stage 1, the gas permeability is measured by using nitrogen with different mean pore pressures. In Stage 2, the thin section analysis and the PMI are conducted to analyze the pore-throat structures of corresponding core samples.

2.3.1. Gas Permeability Measurement

Prior to each gas permeability measurement, the porosity of the core samples is measured through a Boyle's law double-cell porosimeter (HZ-K16, Xi'an, China) with a relative error of less 2%. Thereafter, the gas permeabilities of 56 core samples were measured at five different mean pore pressures. More specifically, nitrogen is injected into core samples with five different inlet pressures of 0.36, 0.50, 0.61, 0.75, and 1.01 MPa, respectively; however, the pressure drops are maintained as 0.26 MPa by adjusting the BPR throughout all of the measurements. With Darcy's law, gas permeabilities can be calculated by using inlet and outlet pressures, and the gas flow rate, through following Equation (1):

$$k_g = \frac{2Q_0 p_0 \mu L}{A\left(p_1^2 - p_2^2\right)} \tag{1}$$

Due to the influences of the slippage effect, the relationship between the measured gas permeability k_g and $1/p_{av}$ is a straight line expressed by Gao et al. [26]:

$$k_g = k_\infty \left(1 + \frac{B}{p_{av}}\right) \tag{2}$$

where B is the Klinkenberg constant. The intercept of such a straight line at the k_g axis is the Klinkenberg permeability, k_∞, i.e., the so-called absolute permeability. It can be determined through the extrapolation of the measured gas permeability to a point where $1/p_{av} = 0$.

2.3.2. PMI Experiments and Thin Section Analysis

In Stage 2, each core sample used in Stage 1 was divided into two parts to separately conduct PMI experiments and thin section analysis for comprehensively analyzing the pore-throat structures. To fit the scales of the PMI setups, the first half of each core sample was trimmed into a reasonable

shape, with diameters and lengths of 25.00 mm. The maximum mercury intrusion pressure was set at 100.00 MPa, corresponding to a throat radius of 7.40 nm, and the equilibrium time for each testing pressure was 90 s. Moreover, the mercury extrusion curves were also measured. Considering that the interfacial tension between air and mercury (σ) is 0.48 N/m and the contact angle (θ) is 140° [19], the capillary pressure curve was converted into throat size distribution curve by using the following equation [20]:

$$p_c = 2\sigma \cos \theta / r_c \tag{3}$$

The second half of each core sample was sliced to obtain thin sections with a thickness of 0.03 mm. Such thin sections were impregnated with blue or red epoxy resin for the visualization of pores and throats. Subsequently, the aforementioned polarizing microscope was equipped to determine particle compositions by applying polarized and cross-polarized analysis. Pore-throat distribution, clay mineral distribution, and grain size could be extracted by analyzing the observation from the polarized light microscope.

3. Results and Discussions

3.1. Experimental Measurements

The measured gas permeabilities under different mean pore pressures and determined Klinkenberg permeability of 50 core samples have been summarized in Table 1. Due to the small pressure drop of 0.26 MPa and the corresponding low flow rate, the non-Darcy flow effect is assumed to be negligible. Note that Sample #8 is used as a representative to demonstrate the experimental results, since its Klinkenberg permeability of 0.070 mD is the closest to the average Klinkenberg permeability of 0.069 mD. Figure 3 illustrates the measured gas permeability versus the inverse of mean pore pressure. A highly satisfactory regression of the measured data has been obtained, with a coefficient of determination of 0.9950. By extrapolating the regression line to the k_g axis, the Klinkenberg permeability of Sample #8 was determined to be 0.070 mD. From the microscopic view of point, the different velocity profiles of fluid and gas flow as shown in Figure 4 are responsible for the differences between the measured gas permeability and the determined Klinkenberg permeability.
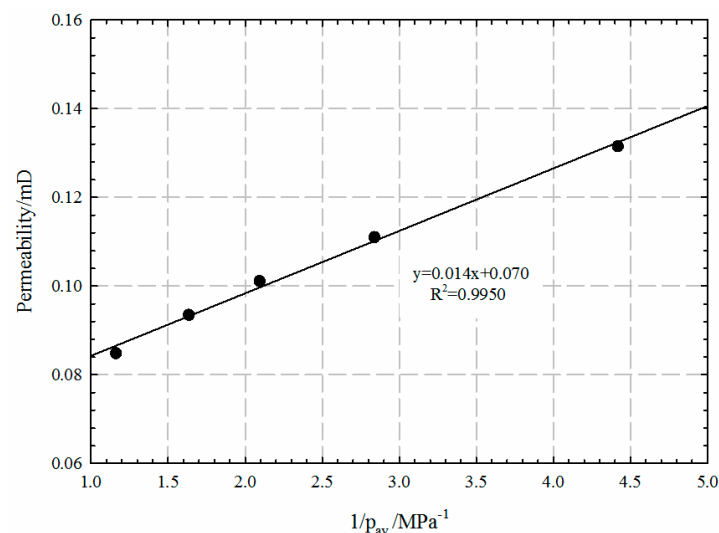

Figure 3. Measured gas permeability versus inverse of pressure for Sample #8.

Table 1. Physical property and pore-throat structure parameters of core samples.

| Samples Number	Gas Permeabilities at Different Mean Pore Pressure * (mD)					Klinkenberg Permeability (mD)	Porosity (%)	Characteristic Parameters of Capillary Pressure Curve				Pore-Throat Type
	0.230 MPa	0.370 MPa	0.480 MPa	0.620 MPa	0.880 MPa			Threshold Capillary Pressure (MPa)	Median Saturation Pressure (MPa)	Maximum Mercury Injection Saturation (%)	Mean Pore-Throat Radius (μm)	
#1	0.016	0.012	0.010	0.009	0.007	0.004	7.34	1.026	21.643	85.95	0.086	BSMT
#2	0.093	0.073	0.065	0.058	0.053	0.039	9.49	0.713	4.269	89.95	0.209	MSMFT
#3	0.215	0.179	0.155	0.144	0.130	0.101	15.44	0.495	2.732	89.07	0.341	GSMFT
#4	0.161	0.136	0.123	0.115	0.108	0.089	15.95	0.558	13.976	86.40	0.104	BSMT
#5	0.136	0.118	0.107	0.102	0.093	0.079	14.64	0.545	8.738	91.05	0.158	BSMT
#6	0.185	0.153	0.142	0.131	0.123	0.120	13.16	1.024	9.419	89.01	0.118	BSMT
#7	0.104	0.083	0.073	0.067	0.059	0.044	13.24	1.083	9.765	80.63	0.107	BSMT
#8	0.132	0.111	0.101	0.094	0.085	0.070	10.85	0.355	2.539	88.20	0.361	GSMFT
#9	0.170	0.141	0.125	0.114	0.096	0.075	10.67	0.342	2.658	88.69	0.359	GSMFT
#10	0.216	0.185	0.168	0.158	0.145	0.121	10.13	0.345	2.548	87.30	0.357	GSMFT
#11	0.304	0.266	0.248	0.234	0.226	0.189	13.43	0.338	2.663	87.15	0.344	GSMFT
#12	0.192	0.175	0.162	0.152	0.134	0.119	12.52	0.342	2.055	87.71	0.475	GSMFT
#13	0.082	0.070	0.061	0.057	0.051	0.041	7.34	0.713	2.672	89.20	0.343	GSMFT
#14	0.114	0.098	0.090	0.084	0.075	0.064	11.89	0.714	13.936	90.21	0.146	MSMFT
#15	0.071	0.057	0.051	0.048	0.044	0.035	7.84	0.712	5.319	86.00	0.190	MSMFT
#16	0.168	0.144	0.132	0.121	0.113	0.095	10.04	0.716	3.660	88.75	0.253	MSMFT
#17	0.100	0.086	0.073	0.067	0.059	0.046	9.79	0.714	13.548	92.70	0.120	BSMT
#18	0.140	0.117	0.101	0.093	0.078	0.060	13.32	0.498	3.545	89.91	0.327	GSMFT
#19	0.261	0.218	0.200	0.188	0.169	0.140	13.93	0.494	2.603	85.62	0.382	GSMFT
#20	0.151	0.133	0.118	0.110	0.101	0.085	13.62	0.714	3.412	89.17	0.303	GSMFT
#21	0.092	0.073	0.065	0.057	0.050	0.037	6.44	0.483	2.611	86.61	0.383	GSMFT
#22	0.135	0.111	0.101	0.093	0.084	0.067	8.85	0.465	4.933	84.69	0.231	MSMFT
#23	0.105	0.088	0.074	0.070	0.063	0.047	9.98	0.723	14.236	92.50	0.119	BSMT
#24	0.165	0.143	0.132	0.124	0.113	0.097	11.39	1.023	7.058	86.54	0.245	MSMFT
#25	0.095	0.080	0.070	0.066	0.056	0.045	12.58	0.511	17.019	86.69	0.098	BSMT
#26	0.052	0.041	0.038	0.033	0.030	0.023	7.02	0.714	5.994	86.34	0.157	MSMFT
#27	0.079	0.064	0.053	0.046	0.042	0.027	9.26	0.713	5.942	82.48	0.198	MSMFT
#28	0.147	0.121	0.111	0.104	0.092	0.075	13.92	0.735	17.156	84.12	0.091	BSMT
#29	0.097	0.079	0.072	0.066	0.058	0.046	9.83	0.712	4.362	92.17	0.200	MSMFT
#30	0.114	0.096	0.088	0.080	0.073	0.060	9.69	0.711	2.713	87.25	0.324	GSMFT
#31	0.034	0.027	0.024	0.021	0.019	0.014	10.85	1.026	10.382	88.48	0.099	BSMT
#32	0.144	0.116	0.107	0.101	0.089	0.071	11.50	0.496	5.122	87.69	0.228	MSMFT
#33	0.145	0.111	0.102	0.095	0.084	0.062	11.50	1.158	10.561	88.59	0.096	BSMT
#34	0.228	0.201	0.187	0.178	0.162	0.142	9.43	0.347	2.373	88.38	0.406	GSMFT
#35	0.093	0.073	0.065	0.058	0.053	0.039	9.49	0.356	2.366	88.56	0.415	GSMFT
#36	0.273	0.241	0.223	0.214	0.195	0.172	9.79	0.494	2.065	84.56	0.413	GSMFT
#37	0.188	0.158	0.141	0.129	0.113	0.092	10.78	0.496	3.128	91.58	0.293	GSMFT
#38	0.147	0.125	0.118	0.108	0.098	0.084	14.01	0.619	17.239	85.91	0.089	BSMT
#39	0.100	0.080	0.070	0.065	0.058	0.043	11.53	0.598	17.125	86.53	0.094	BSMT
#40	0.160	0.130	0.120	0.109	0.091	0.073	13.97	0.585	17.028	86.67	0.095	BSMT
#41	0.118	0.095	0.084	0.077	0.068	0.052	10.57	0.902	16.522	91.38	0.109	BSMT
#42	0.078	0.061	0.055	0.049	0.044	0.033	9.17	0.695	16.513	91.26	0.107	BSMT
#43	0.007	0.005	0.004	0.004	0.003	0.002	6.44	0.686	16.429	91.63	0.102	BSMT
#44	0.123	0.107	0.096	0.088	0.080	0.067	12.10	0.715	4.797	91.81	0.236	MSMFT
#45	0.146	0.118	0.107	0.101	0.090	0.071	13.67	0.499	2.172	88.91	0.404	GSMFT
#46	0.081	0.068	0.061	0.055	0.050	0.040	11.56	0.713	5.570	91.82	0.184	MSMFT
#47	0.048	0.039	0.036	0.033	0.030	0.025	7.10	0.715	13.884	89.75	0.154	MSMFT
#48	0.100	0.083	0.077	0.071	0.066	0.055	8.90	0.495	12.537	89.97	0.176	MSMFT
#49	0.136	0.110	0.103	0.096	0.087	0.071	9.96	0.495	7.560	85.97	0.147	MSMFT
#50	0.150	0.131	0.118	0.112	0.100	0.085	11.73	0.716	5.408	88.12	0.242	MSMFT

* Measured with nitrogen.
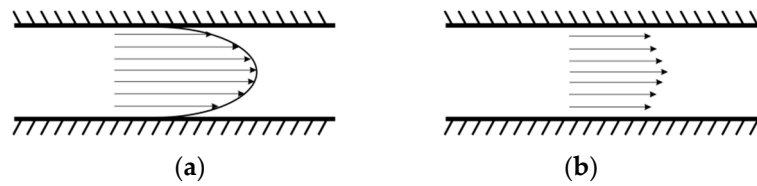
Figure 4. Schematic diagram of gas slippage effect: (**a**) Liquid flow through a capillary; (**b**) Gas flow through a capillary [2].

The mercury intrusion curve of Sample #29 is shown in Figure 5, where characteristic parameters, such as threshold capillary pressure p_{ct}, median saturation pressure p_{c50}, and maximum saturation of mercury injection S_{max} have been marked to demonstrate the pore-throat structure of each core sample. In addition, average throat radius can be calculated by using the following equation [27]:

$$r_{av} = \frac{\sum (r_{i+1} + r_i)(S_{i+1} - S_i)}{2 \sum (S_{i+1} - S_i)} \tag{4}$$
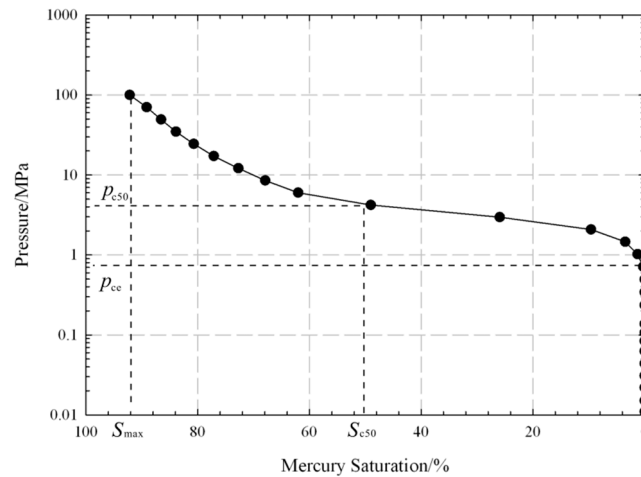
Figure 5. Capillary pressure curve of Sample #29.

As such, the pore-throat structure can be explicitly represented by those quantitative parameters to a certain degree, which provides a convenient manner to investigate the effect of the pore-throat structure on the Klinkenberg permeability. Therefore, the characteristic parameters of all core samples have been measured and tabulated in Table 1.

It has been found that the Klinkenberg permeabilities range from 0.002 to 0.189 mD. As for Samples #39 and #48, the measured gas permeability is the same for both of them when the same mean pore pressure of 0.230 MPa is applied; however, the Klinkenberg permeabilities of them have a difference of 27.91%. This variation in the Klinkenberg permeability is attributed to the different pore-throat structure represented by the various characteristic parameters of the two samples (see Table 1). In addition, the effect of the pore-throat structure, i.e., the characteristic parameters of capillary pressure curves, on the Klinkenberg permeability can be found from other core samples, as shown in Table 1.

3.2. Pore-Throat Structure Type

It has been addressed that the capillary pressure curve exhibits various shapes for core samples with distinctly different pore-throat structures [28]. In the present work, the results of PMI measurement and thin section analysis are used to classify the pore-throat structure of 56 core

samples. According to the different shapes of three representative capillary curves and corresponding characteristic parameter, as shown in Figure 6, the pore-throat structure can be represented by three types: good sorting and micro-fine throat (GSMFT), moderate sorting and micro-fine throat (MSMFT), and bad sorting and micro throat (BSMT). The last column of Table 1 indicates the pore-throat structure type of each core sample, while the characteristic parameters of the three types are summarized and tabulated in Table 2. From the perspective of quantitative differentiation, the mean throat radius can be used as a criterion discriminating three types of pore-throat structure. As for the fluid flow or production performance, the GSMFT type curve is the most favored one, with its low pore-throat sorting coefficient indicating the uniform level of the pore-throat distribution, low capillary pressure, and high maximum mercury injection saturation. On the contrary, the BSMT type curve is not anticipated, due to a high sorting coefficient implying a large amount of nano-sized throats. The pore-throat sorting coefficient is determined by the equation:

$$S_p = \frac{\Phi_{84} - \Phi_{16}}{4} + \frac{\Phi_{95} - \Phi_5}{6.6} \tag{5}$$

where S_p is the pore-throat sorting coefficient; $\Phi_i = -\log_2 d_i$; d_i is the pore, and throat diameter is represented by μm.
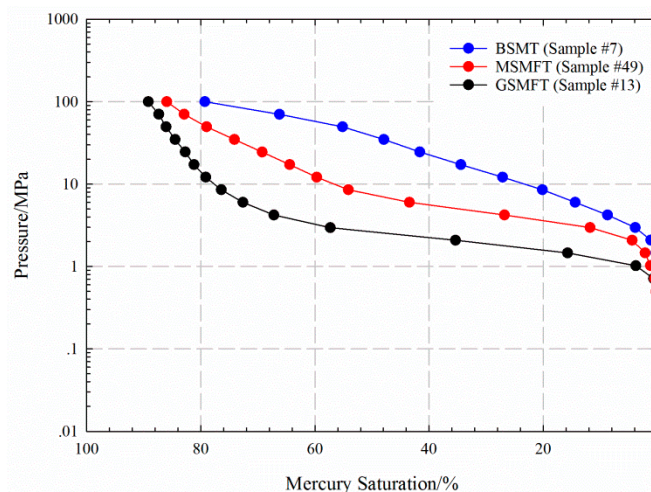

Figure 6. Representative capillary pressure curves of the good sorting and micro-fine throat (GSMFT), moderate sorting and micro-fine throat (MSMFT), and bad sorting and micro throat (BSMT) types of pore-throat structure.

Table 2. Characteristic parameters of different pore-throat structure types.

Type	Pore-Throat Sorting Coefficient	Entry Pressure (MPa)	Median Saturation Pressure (MPa)	Mean Throat Radius (μm)	Maximum Mercury Injection Saturation (%)
GSMFT	1.175–2.027	0.338–0.714	2.05–3.55	0.293–0.475	84.56–92.70
MSMFT	1.308–2.133	0.465–1.023	3.66–13.94	0.146–0.253	82.48–92.17
BSMT	1.583–2.788	0.511–1.464	8.74–39.03	0.070–0.158	79.30–91.58

According to the results of thin section analysis, the particle composition and pore type of the core samples are identified. The classification triangle [29] of quartz, feldspar, and rock fragments has been established, and shown in Figure 7. It can be found that the lithology of all three types of pore-throat structures falls into arkose and lithic arkose. As shown in Figure 8a, fine sand and very fine sand are the majority of all three types of pore-throat structure. The pore types are specified with the assistance of the thin section analysis, and have been expressed in Figure 8b. From the BSMT to GSMFT type of pore-throat structure, the percentage of the intergranular pores gradually increases; meanwhile, the

percentage of the intercrystalline pore decreases until zero. The changes in the ratios of different pores prove that it is necessary to separately handle these pore-throat structures for the purpose of accuracy.
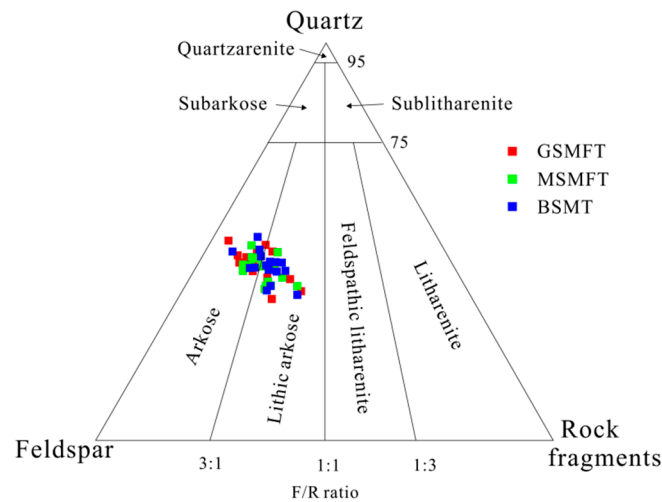

Figure 7. Particle composition of three pore-throat structure types plotted on the classification triangle.
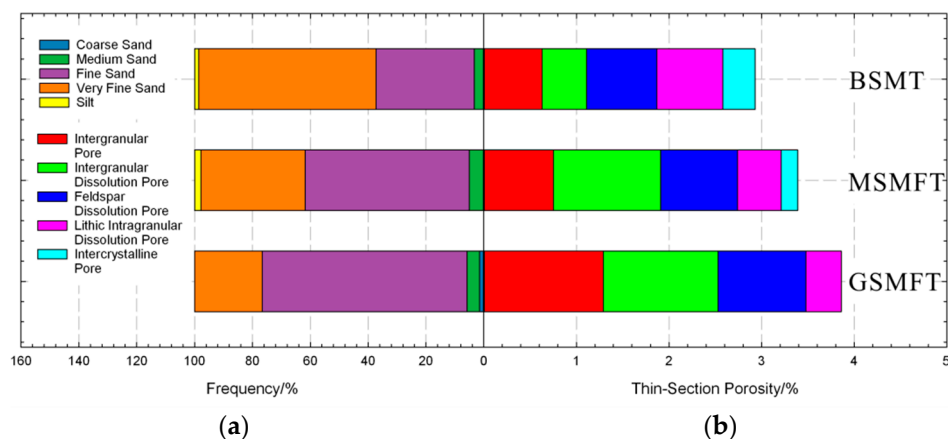

Figure 8. (**a**) Grain size and (**b**) pore types distribution of three pore-throat structure types obtained from thin section analysis.

The different features of these three types of pore-throat structure can also be found from the electronic images of the slices of core samples. As for the GSMFT type of pore-throat structure, the image of intergranular pores and intergranular dissolution pores is shown in Figure 9. It can be directly observed that these two types of pores are dominant among the five presented pore types in Figure 8b. Quantitatively, the GSMFT type of pore-throat structure is featured in the low threshold capillary pressure, which ranges from 0.338 to 0.714 MPa. In addition, the thin-section porosity of the GSMFT type of pore-throat structure is larger than that of other two types of the pore-throat structure by 3.86% on average. Regarding the MSMFT type of pore-throat structure, intergranular dissolution pores and feldspar dissolution pores (see Figure 10) are the main pore types. Due to the enhancement of compaction and cementation, feldspar dissolution pores and lithic intergranular dissolution pores, as shown in Figure 11, are predominant for the BSMT types of pore-throat structure. The existence of a large amount of nano-scale throats induces the lower thin-section porosity of 2.93% and the higher median saturation pressure up to 21.643 MPa.
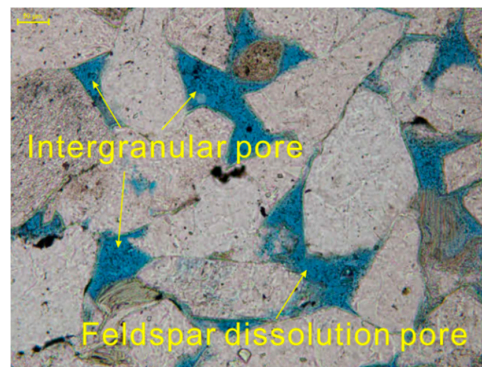
Figure 9. Intergranular pore and feldspar dissolution pore of the GSMFT type of pore-throat structure (Sample #11).
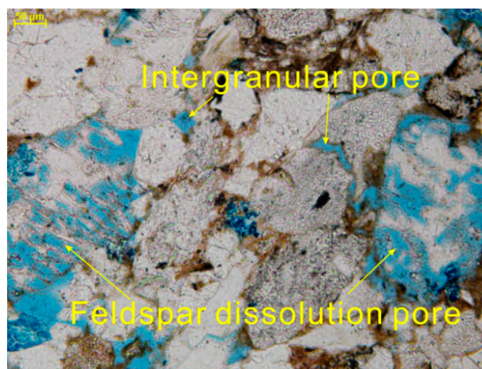

Figure 10. Feldspar dissolution pore and intergranular pore of the MSMFT type of pore-throat structure (Sample #16).
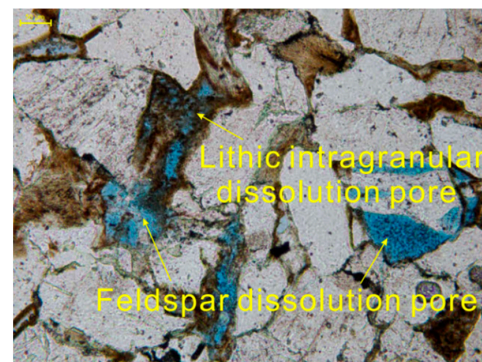

Figure 11. Feldspar dissolution pore and lithic intragranular dissolution pore of the BSMT type of pore-throat structure (Sample #42).

3.3. Klinkenberg Permeability

In general, the slippage effect appears when the mean free path of the measuring gas molecules is greater than the throat diameters. As such, the Klinkenberg constant describing the difference between measured gas permeability and Klinkenberg permeability is dramatically impacted by the pore-throat structure of core samples. Figure 12a–c shows the linear relationships between Klinkenberg permeability and measured gas permeability at different mean pore pressure for the three pore-throat structure types, respectively. Those linear relationships can be mathematically represented by:
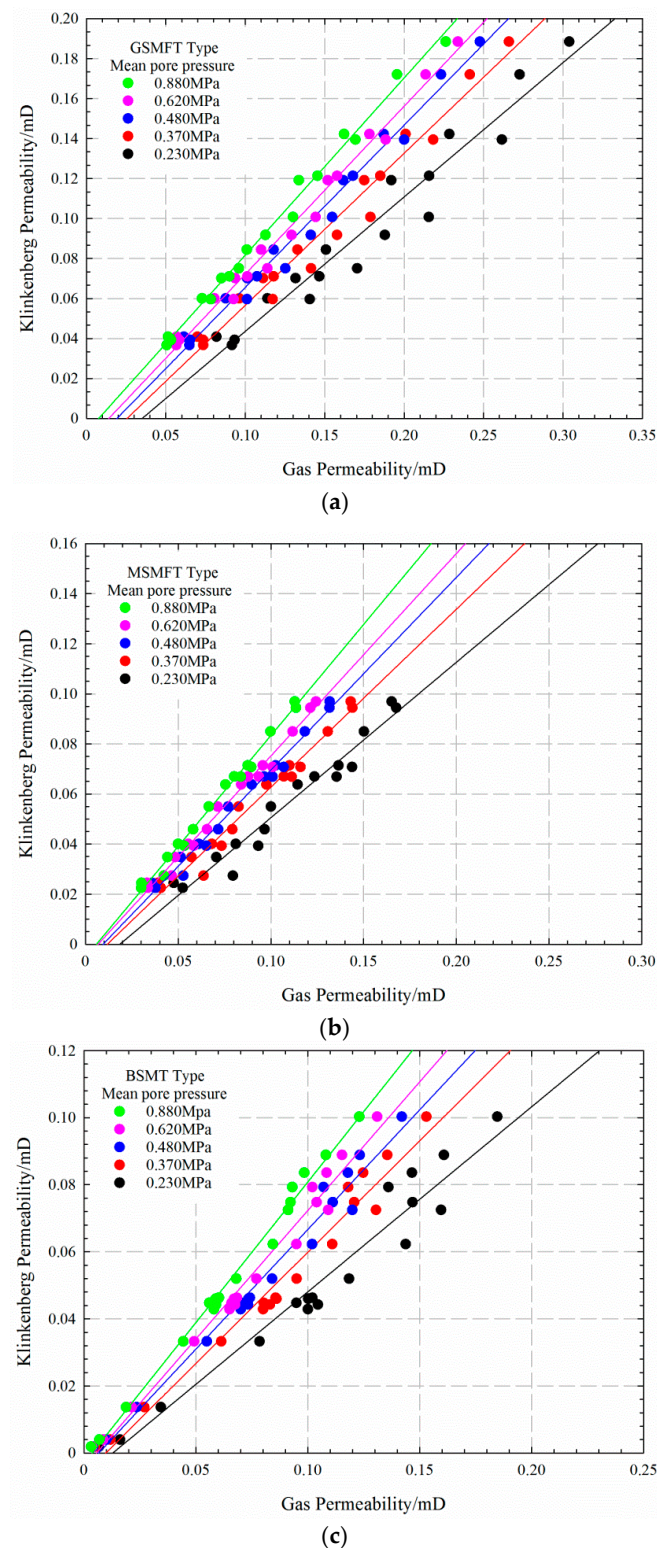
$$k_\infty = ak_g + b \tag{6}$$

Figure 12. Klinkenberg permeability versus gas permeability for different pore-throat structure types: (**a**) GSMFT, (**b**) MSMFT, and (**c**) BSMT.

The values of the slope *a* and the intercept *b* have been inversely determined and listed in Table 3 by fitting the measured data. For the same type of pore-throat structure, both the slope and the intercept increase significantly with the mean pore pressure. At the same mean pore pressure, the slopes decreases and the intercept increase, while the pore throat structure deteriorates.

Table 3. Estimated slopes and intercepts for three pore-throat structure types at different mean pore pressures.

| Type	Parameter	Mean Pore Pressure (MPa)				
		0.230	**0.370**	**0.480**	**0.620**	**0.880**
GSMFT	slope	0.6718	0.7430	0.7985	0.8333	0.8858
	intercept	−0.0235	−0.0164	−0.0135	−0.0108	−0.0068
MSMFT	slope	0.6205	0.7064	0.7606	0.8021	0.8723
	intercept	−0.0115	−0.0079	−0.0065	−0.0050	−0.0041
BSMT	slope	0.5578	0.6602	0.7133	0.7663	0.8384
	intercept	−0.0079	−0.0061	−0.0047	−0.0040	−0.0030

It is worthwhile to note that the intercepts of these curves are negative for all three types of pore-throat structure in the tight formation. Physically, the liquid permeability may not be measured due to the existence of fluid film attached to rock surface, which resulted from the small pore-throat size, the complex pore-throat structure, and the large solid–liquid interfacial force in a tight formation [30]. However, the gas permeability can be measured at a similar condition because of the gas slippage effect. This implies that the negative intercepts or the points of intersection on the abscissa axis (see Figure 12) is possible to be observed while the pore-throat is extremely small in tight formations. In addition, the negative intercepts further indicate the effects of the pore-throat structure on the determination of the absolute permeability of the tight formation.

The slopes and intercepts of three types of pore-throat structure have been plotted against the mean pore pressure, as shown in Figure 13. It can be found that the relationship between the slope/intercept and the mean pore pressure can be represented by a power function, i.e., $a(\text{or } b) = mp_{av}^n$. Figure 13 shows the fitting lines to the measured data with the coefficients of determination larger than 0.9858. The values of m and n have been regressively determined, and the power functions are combined with Equation (6), which generate three empirical equations for the three types of pore-throat structure, as following:

$$\text{GSMFT equation}: \ k_\infty = \left(0.9174 p_{av}^{0.2084}\right) k_g - 0.007 p_{av}^{-0.834} \tag{7a}$$

$$\text{MSMFT equation}: \ k_\infty = \left(0.9095 p_{av}^{0.2513}\right) k_g - 0.003 p_{av}^{-0.795} \tag{7b}$$

$$\text{BSMT equation}: \ k_\infty = \left(0.8844 p_{av}^{0.2954}\right) k_g - 0.002 p_{av}^{-0.691} \tag{7c}$$
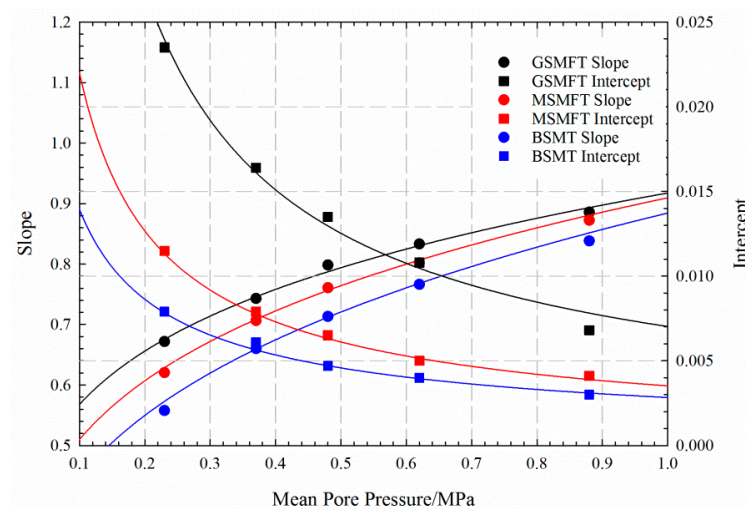
Figure 13. Slope and intercept versus mean pore pressure for different pore-throat structure types.

To demonstrate the performance of these derived equations, the absolute permeabilities of Samples #51–56 are calculated by using all three equations. The measurements and calculation results of Samples #51–56 have been summarized in Table 4, while an error analysis diagram has been shown in Figure 14. Since the pore-throat structure of Sample #53 is the MSMFT type, the MSMFT equation generates the best estimation of the Klinkenberg permeability, with a relative error of 4.00%, while the GSMFT and BSMT equations yield relative errors of 24.00% and 6.00%, respectively. This implies that the accurate determination of the Klinkenberg permeability requires an appropriate equation for a specific type of pore-throat structure. Note that the proposed correlations are solely useful for their corresponding types of pore structure. The coefficients need to be further modified for extending the applicability of the proposed correlations to different formations.

Table 4. The measurements and calculated results of Klinkenberg permeability.

| Samples Number | Type | Mean Pore Pressure (MPa) | Measured Results | | Calculated Results and Relative Error with Measured Results | | | | | |
			Gas Permeability (mD)	Klinkenberg Permeability (mD)	GSMFT Equation		MSMFT Equation		BSMT Equation	
					Klinkenberg Permeability (mD)	Relative Error (%)	Klinkenberg Permeability (mD)	Relative Error (%)	Klinkenberg Permeability (mD)	Relative Error (%)
#51	GSMFT	0.230	0.147	0.073	0.075	2.74	0.082	12.33	0.078	6.85
#52			0.207	0.117	0.116	0.85	0.120	2.56	0.113	3.42
#53	MSMFT	0.230	0.092	0.050	0.038	24.00	0.048	4.00	0.047	6.00
#54			0.103	0.054	0.046	14.81	0.055	1.85	0.053	1.85
#55	BSMT	0.230	0.144	0.076	0.074	2.63	0.077	1.32	0.077	1.32
#56			0.094	0.047	0.040	14.89	0.050	6.38	0.048	2.13
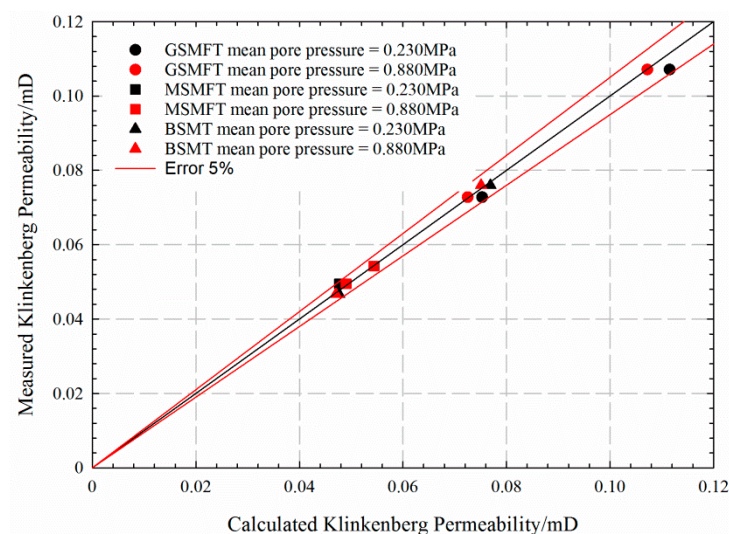
Figure 14. Calculated Klinkenberg permeability using equations versus measured Klinkenberg permeability.

The performance of the derived equations is further demonstrated by Figure 14, which demonstrates through properly using the derived empirical equations that the difference between measured and calculated Klinkenberg permeability is less than 5%. Consequently, those derived equations can be used to determine the absolute permeability of a tight formation sharing similar characteristic parameters with three types of the pore-throat structure defined in this work. Moreover, the Klinkenberg permeability-gas permeability chart has been obtained from Equation (7) for the GSMFT, MSMFT, and BSMT types of pore-throat structure, respectively, as shown in Figure 15. It is convenient to determine the Klinkenberg permeability, even if there is only one measure gas permeability, as it provides a great tool for the reservoir engineers to efficiently estimate the permeability of tight formations.
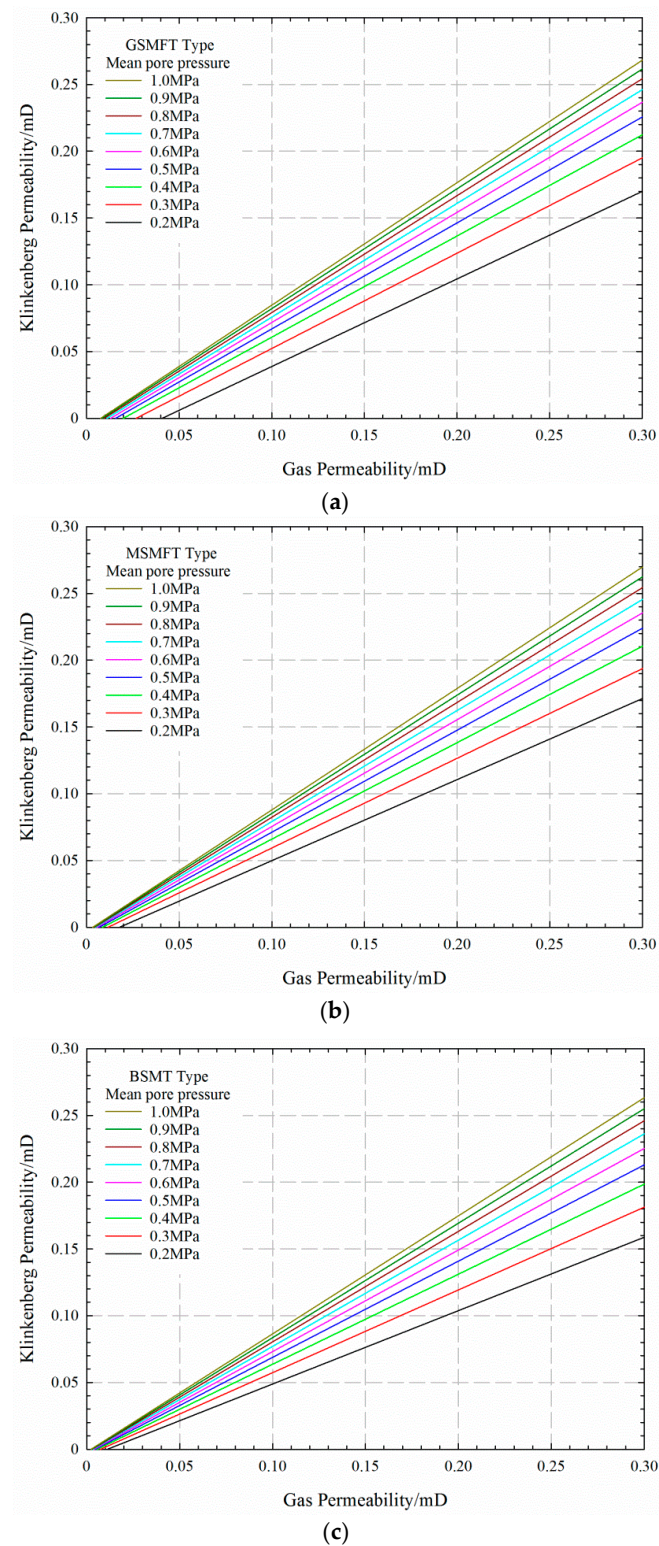
Figure 15. Klinkenberg permeability-gas measure permeability chart for different pore-throat structure types: (**a**) GSMFT, (**b**) MSMFT, and (**c**) BSMT.

4. Conclusions

A pragmatic technique including three empirical equations has been proposed to determine the Klinkenberg permeability through considering the pore-throat structure, mean pore pressure,

and measured gas permeability. Based on the measured data of 50 core samples, the Klinkenberg permeability is linearly related to the measured gas permeability, and the coefficients of such a linear relationship can be regressively determined. The results of PMI experiments and thin section analyses indicate that the pore-throat structure of the given tight formation can be categorized into three types, i.e., GSMFT, MSMFT, and BSMT. The different features of these three types of pore-throat structure can be found from both the capillary pressure curves and the electronic images of the slices of core samples.

After considering the classified pore-throat structure, the dependence of the Klinkenberg permeability on the measured gas permeability has been mathematically expressed by empirical GSMFT, MSMFT, and BSMT equations, respectively. The effects of mean pore pressure and measured gas permeability are explicitly represented, while the impact of the pore-throat structure is implicitly described by the coefficients in the equations. It has been found that the application of a GSMFT equation to a MSMFT type of pore-throat structure yields a corrupted estimate of the Klinkenberg permeability with a relative error of 24.0%, which can be decreased to 4.0% by applying the MSMFT equation to a MSMFT type of pore throat structure. This implies that it is of significant importance to use the appropriate equation to determine the Klinkenberg permeability of a specific tight formation. Overall, the relative error of the calculated Klinkenberg permeability using the proposed three empirical equations is less than 5.0% in comparison to measured values. Consequently, the newly proposed technique provides a pragmatic tool for reservoir engineers to accurately and efficiently determine the Klinkenberg permeability with limited measured data.

Author Contributions: Guangfeng Liu and Yaoxing Bai conceived and designed the experiments; Yaoxing Bai performed the experiments; Guangfeng Liu and Zhaoqi Fan analyzed the data; Daihong Gu contributed reagents, materials and analysis tools; Guangfeng Liu, Yaoxing Bai, Zhaoqi Fan and Daihong Gu wrote the paper.

Conflicts of Interest: The authors declare no conflict of interest.

Nomenclature

Notations

A	cross-sectional area of the core sample, cm^2.
B	Klinkenberg constant, MPa.
d_i	throat radius, μm.
k_g	gas permeability, mD.
k_∞	absolute permeability, mD.
L	length of the core sample, cm.
p_0	atmospheric pressure, 100 kPa.
p_1, p_2	the absolute pressures of inlet and outlet respectively, 100 kPa.
p_{av}	mean flow pressure (equal to $(p_1 + p_2)/2$), MPa.
p_c	capillary pressure, MPa.
Q_0	volumetric flow rate at the standard condition, cm^3/s.
r_{av}	average pore radius, μm.
r_c	throat radius, μm.
r_i	throat radius, μm.
s_i	cumulative mercury saturation of throat radius r_i.
S_p	pore-throat sorting coefficient.

Greek Letter

μ	gas viscosity, mPa·s.

References

1. Wu, K.L.; Chen, Z.X.; Li, X.F.; Xu, J.Z.; Wang, K.; Wang, H.; Wang, S.H.; Dong, X.H. Flow behavior of gas confined in nanoporous shale at high pressure: Real gas effect. *Fuel* **2017**, *205*, 173–183. [CrossRef]
2. He, G.; Tang, H. *Petrophysics*, 2nd ed.; Petroleum Industry Press: Beijing, China, 2011; pp. 57–62. ISBN 978-7-5021-8424-7.
3. Tiab, D.; Donaldson, E.C. *Petrophysics: Theory and Practice of Measuring Reservoir Rock and Fluid Transport Properties*, 2nd ed.; Gulf Professional Publishing: Burlington, NJ, USA, 2004; pp. 822–825, ISBN 0-7506-7711-2.
4. Zhu, G.Y.; Liu, X.G.; Li, S.T.; Huang, Y.Z.; Hao, M.Q. A study of slippage effect of gas percolation in low permeability gas pools. *Nat. Gas Ind.* **2007**, *27*, 44–47.
5. Zhu, W.Y.; Song, H.Q.; He, D.B.; Wang, M.; Jia, A.L.; Hu, Y.L. Low-velocity non-Darcy gas seepage model and productivity equation of low-permeability water-bearing gas reservoir. *Nat. Gas Geosci.* **2008**, *19*, 685–689.
6. Klinkenberg, L. The permeability of porous media to liquids and gases. In Proceedings of the Drilling and Production Practice, New York, NY, USA, 1 January 1941.
7. Wu, K.L.; Chen, Z.X.; Li, J.; Li, X.F.; Xu, J.Z.; Dong, X.H. Wettability effect on nanoconfined water flow. *Proc. Natl. Acad. Sci. USA* **2017**, *114*, 3358–3363. [CrossRef] [PubMed]
8. Sampath, K.; Keighin, C.W. Factors affecting gas slippage in tight sandstones of cretaceous age in the Uinta basin. *J. Pet. Technol.* **1982**, *34*, 2715–2720. [CrossRef]
9. Rushing, J.; Newsham, K.; Van Fraassen, K. Measurement of the two-phase gas slippage phenomenon and its effect on gas relative permeability in tight gas sands. In Proceedings of the SPE Annual Technical Conference and Exhibition, Denver, CO, USA, 5–8 October 2003.
10. Al-Bulushi, I.R.; Al-Maamari, R.S.; Wilson, O.B. Brine versus Klinkenberg corrected gas permeability correlation for Shuaiba carbonate formation. *J. Pet. Sci. Eng.* **2012**, *92–93*, 24–29. [CrossRef]
11. Wu, K.L.; Li, X.F.; Wang, C.C.; Yu, W.; Chen, Z.X. Model for Surface Diffusion of Adsorbed Gas in Nanopores of Shale Gas Reservoirs. *Ind. Eng. Chem. Res.* **2015**, *54*, 3225–3236. [CrossRef]
12. Wu, K.L.; Li, X.F.; Guo, C.H.; Wang, C.C.; Chen, Z.X. A Unified Model for Gas Transfer in Nanopores of Shale-Gas Reservoirs: Coupling Pore Diffusion and Surface Diffusion. *SPE J.* **2016**, *21*, 1–29. [CrossRef]
13. Letham, E.A.; Bustin, R.M. Klinkenberg gas slippage measurements as a means for shale pore structure characterization. *Geofluids* **2016**, *16*, 264–278. [CrossRef]
14. Li, J.; Sultan, A.S. Klinkenberg slippage effect in the permeability computations of shale gas by the pore-scale simulations. *J. Nat. Gas Sci. Eng.* **2016**, in press. [CrossRef]
15. Aguilera, R. Flow Units: From Conventional to Tight-Gas to Shale-Gas to Tight-Oil to Shale-Oil Reservoirs. *SPE Reserv. Eval. Eng.* **2014**, *17*, 190–208. [CrossRef]
16. Chen, D. Gas slippage phenomenon and change of permeability when gas flows in tight porous media. *Acta Mech. Sin.* **2002**, *34*, 96–100.
17. Zhu, Y.H.; Tao, G.; Fang, W.; Wang, S.K. Research progress of the Klinkenberg Effect in Tight Gas Reservoir. *Prog. Geophys.* **2007**, *22*, 1591–1596.
18. Ashrafi Moghadam, A.; Chalaturnyk, R. Expansion of the Klinkenberg's slippage equation to low permeability porous media. *Int. J. Coal Geol.* **2014**, *123*, 2–9. [CrossRef]
19. Dong, J.; Tong, M.; Ran, B.; Li, N. Nonlinear percolation mechanisms in different storage-percolation modes in volcanic gas reservoirs. *Pet. Explor. Dev.* **2013**, *40*, 372–377. [CrossRef]
20. Lai, J.; Wang, G.; Ran, Y.; Zhou, Z.; Cui, Y. Impact of diagenesis on the reservoir quality of tight oil sandstones: The case of Upper Triassic Yanchang Formation Chang 7 oil layers in Ordos Basin, China. *J. Pet. Sci. Eng.* **2016**, *145*, 54–65. [CrossRef]
21. Xi, K.; Cao, Y.; Haile, B.G.; Zhu, R.; Jahren, J.; Bjørlykke, K.; Zhang, X.; Hellevang, H. How does the pore-throat size control the reservoir quality and oiliness of tight sandstones? The case of the Lower Cretaceous Quantou Formation in the southern Songliao Basin, China. *Mar. Pet. Geol.* **2016**, *76*, 1–15. [CrossRef]
22. China Standards Publication. *Practices for Core Analysis*; GB/T29172-2012; China Standards Press: Beijing, China, 2012; pp. 1–238.
23. Wang, M.; Zhang, S.A.; Zhang, F.; Liu, Y.; Guan, H.; Li, J.; Shao, L.; Yang, S.; She, Y. Quantitative research on tight oil microscopic state of Chang 7 Member of Triassic Yanchang Formation in Ordos Basin, NW China. *Pet. Explor. Dev.* **2015**, *42*, 827–832. [CrossRef]

24. Liu, F.; Zhu, X.; Li, Y.; Xu, L.; Niu, X.; Zhu, S.; Liang, X.; Xue, M.; He, J. Sedimentary characteristics and facies model of gravity flow deposits of Late Triassic Yanchang formation in southwestern Ordos Basin, NW China. *Pet. Explor. Dev.* **2015**, *42*, 633–645. [CrossRef]

25. Wu, K.; Chen, Z.; Li, X.; Guo, C.; Wei, M. A model for multiple transport mechanisms through nanopores of shale gas reservoirs with real gas effect-adsorption-mechanic coupling. *Int. J. Heat Mass Transf.* **2016**, *93*, 408–426. [CrossRef]

26. Gao, H.; Li, H.A. Pore structure characterization, permeability evaluation and enhanced gas recovery techniques of tight gas sandstones. *J. Nat. Gas Sci. Eng.* **2016**, *28*, 536–547. [CrossRef]

27. China National Petroleum Corporation. *Rock Capillary Pressure Measurement*; SY/T 5346-2005 Oil and Gas Industry Standard of the People's Republic of China; Petroleum Industry Press: Beijing, China, 2005; pp. 1–17.

28. Yang, S. *Fundamentals of Petrophysics*; Petroleum Industry Press: Beijing, China, 2011; pp. 281–309. ISBN 987-7-5021-7589-4.

29. Zhou, Y.; Ji, Y.; Zhang, S.; Wan, L. Controls on reservoir quality of Lower Cretaceous tight sandstones in the Laiyang Sag, Jiaolai Basin, Eastern China: Integrated sedimentologic, diagenetic and microfracturing data. *Mar. Pet. Geol.* **2016**, *76*, 26–50. [CrossRef]

30. Liu, W.; Liu, J.; Sun, L.; Yang, L.I. Boundary Layer on Fluid Flow in Low Permeability Oilfields. *Sci. Technol. Rev.* **2011**, *29*, 42–44.